Neutral conditions-enabled robust electrocatalytic hydrogenation of biomass-derived furfural using atomically precise nanocluster-based catalysts

Xinhua Yuan[a,b], Fan Yang[a], Ying Lv[a,c], Chen Li[a], Honglei Shen[a], Chongqing Pan[a], Jinhui Hu[a], Xiaolong Wu[a], Rui Diao[d], Chu Wang[e], Qiang Lu[b], Xi Kang[a]*, Haizhu Yu[a]*, Manzhou Zhu[a]**

[a]Department of Chemistry and Centre for Atomic Engineering of Advanced Materials, Anhui Province Key Laboratory of Chemistry for Inorganic/Organic Hybrid Functionalized Materials, Anhui University, Hefei, Anhui 230601, China.

[b]Energy and Power Innovation Research Institute, North China Electric Power University, Beijing 102206, P. R. China.

[c]School of Chemistry and Materials Engineering, Fuyang Normal University, Fuyang 236041, China

[d]School of Mechanical Engineering, Hefei University of Technology, Hefei, Anhui 230009, PR China.

[e]School of Energy and Power Engineering, Dalian University of Technology, Dalian, Liaoning, 116081, PR China.

*E-mails of corresponding authors: qlu@ncepu.edu.cn (Q.L.); kangxi_chem@ahu.edu.cn (X.K.); yuhaizhu@ahu.edu.cn (H.Y.); zmz@ahu.edu.cn (M.Z.)

X.Y., F.Y. and Y.L. contributed equally to this work.

Keywords: furfural, nanocluster, electrocatalytic hydrogenation, neutral condition

Materials and Methods

Materials and chemicals

Unless otherwise specified, all chemicals and reagents were purchased and utilized without any additional processing. Furfural ($C_5H_4O_2$, GR), potassium sulfate (K_2SO_4, AR), deuterium oxide (D_2O, GR), copper acetylacetonate ($Cu(C_5H_7O_2)_2$, GR), silver nitrate ($AgNO_3$, GR), tetrachloroauric (III) acid ($HAuCl_4•3H_2O$, GR), triphenylphosphine (PPh_3, GR), benzene-1,3-dithiol (SSR, GR), sodium borohydride ($NaBH_4$, GR), methylene chloride (CH_2Cl_2, HPLC), methanol (CH_3OH, HPLC), ethanol (CH_3CH_2OH, HPLC), and N,N-dimethylformamide (DMF, HPLC) were purchased from Sigma–Aldrich. According to the literature[1], the synthesis of hydrofuroin was carried out using Mg-mediated homocoupling methods. Nafion solution (5 wt.%) and a Nafion 117 proton exchange membrane were purchased from DuPont. Cu foam (CuF, thickness: 2 mm, porosity: ⩾97%, PPI: 10-130, surface roughness Ra: 0.8-1.8 μm) was purchased from Kunshan Guangjiayuan New Material Co., Ltd. Deionized water was obtained from Anhui University. All electrodes were obtained from GaossUnion Co., Ltd.

Synthesis of the Ag_{29}, $Ag_{17}Cu_{12}$, and $Ag_{16}Cu_{12}Au_1$ nanoclusters

Ag_{29}, $Ag_{17}Cu_{12}$, and $Ag_{16}Cu_{12}Au_1$ were synthesized according to our previous study[2]. Briefly, for the synthesis of Ag_{29}, 20 mg of $AgNO_3$ was dissolved in methanol, and 5 ml of methanol and

10 ml of dichloromethane were then added into the solvent. After the sample was thoroughly mixed, 13.5 μl of BDT and 200 mg of TPP were sequentially added. Subsequently, 10.2 mg of $NaBH_4$ was dissolved in 1 ml of ice water and added to the solution; next, the solution was stirred and allowed to react overnight. Ag_{29} was obtained by washing the product three times with methanol. According to the ratio of metal atoms in different nanoclusters, $Ag_{17}Cu_{12}$ and $Ag_{16}Cu_{12}Au_1$ could be obtained by replacing $AgNO_3$ with the same proportion of $HAuCl_4 \cdot 3H_2O$ and $Cu(C_5H_7O_2)_2$.

Preparation of the working electrodes

The foams of the working electrode were meticulously trimmed to 1.0 cm * 1.5 cm while maintaining a geometric surface area of 1 cm^2 (1.0 cm * 1.0 cm) for the electrocatalytic tests. Then, the Cu foam was subjected to ultrasonic washing in ethanol and hydrochloric acid for 15 min each to eliminate the specified impurities and oxidize the layers. Next, the Cu foam was stored in ethanol. The working electrodes were produced by drop coating. In more detail, 0.5 mg of the nanocluster was dissolved in 1 ml of DMF, and then 35 μl of Nafion solution (5%) was added. The resulting ink was slowly added dropwise onto the surface of the Cu foam to obtain a uniform coating. The obtained electrodes were dried overnight in a vacuum drying oven (60 ℃).

Characterization

An Agilent 8453 diode array spectrometer was used to record all UV−vis absorption spectra of the nanoclusters dissolved in DMF. Electrospray ionization time-of-flight mass spectrometry (ESI-TOF-MS) was conducted using a high-resolution mass spectrometer (MicrOTOF-QIII). SEM was performed using a Regulus 8230 microscope. EDS mapping images were obtained with an EDAX octanesuper microscope. Inductively coupled plasma mass spectrometry (ICP-MS) measurements were carried out on a Thermo Scientific iCAP Qc instrument. For ICP-MS analysis, 1 mL of post-

electrolysis electrolyte was diluted with 9 mL of deionized water and digested with 5 mL of aqua regia (HNO_3:HCl = 1:3) prior to analysis. A Thermo ESCALAB 250 instrument was utilized for the X-ray photoelectron spectroscopy (XPS) measurements. All XPS data presented in the manuscript were charge-corrected using the C 1s peak at 284.8 eV. The instrument consisted of a monochromatic Al Kα (1486.8 eV) 150 W X-ray source, a circular spot size of 0.5 mm, a flood gun to mitigate charging effects, and an analysis chamber base pressure below 1×10^{-9} mbar. Nuclear magnetic resonance (NMR) spectra were obtained using a Bruker 600 Avance III spectrometer equipped with a Bruker BBO multinuclear probe (BrukerBioSpin).

The in situ EPR tests were conducted using a Bruker EMXPlus instrument with a magnetic field range of 3455 G to 3555 G. The microwave frequency was 9.853 GHz, with a modulation amplitude of 1 G and a microwave power of 20 mW. The ATR-SEIRAS test was performed in an in situ infrared electrochemical cell (Hefei in situ Technology Co., Ltd., China), with an infrared signal acquired by a PerkinElmer Spectrum 3. All spectra were collected at a resolution of 4 cm^{-1} in the wavenumber range of 4000-1000 cm^{-1}.

Electrochemical measurements

All electrochemical experiments were conducted with a CHI 760E electrochemical analyzer (CH Instruments, Inc., Shanghai) at room temperature. An H-type cell equipped with a Nafion 117 membrane was utilized for the electrochemical test, employing a three-electrode system with an Ag/AgCl (1 M KCl) reference electrode and a 1*1 cm^2 Pt sheet as the counter electrode. Prior to conducting any additional experiments, N_2 gas was introduced into the electrolyte to eliminate oxygen for 20 min. Moreover, the catalysts were activated using cyclic voltammetry in an electrolyte of 0.5 M K_2SO_4. The scan rate of the CV and LSV tests was set to 100 mV/s. The chronopotentiometry measurements were conducted for 2 hours at the constant potential. The

reported half-cell potentials were manually IR-corrected. Prior to the electrochemical tests, the uncompensated resistance (R_u), primarily comprising the solution and contact resistance, was determined via electrochemical impedance spectroscopy. The IR drop was then calculated using a compensation factor of 90% and subtracted from the measured applied potential to obtain the IR-corrected value. To ensure a fair comparison of catalyst performance, all reported selectivity and FE data in this study were collected after a fixed electrolysis duration of 2 hours, at constant potential.

According to the Nernst equation, the potential vs. Ag/AgCl could be converted to the RHE by the following equation.

$$E\left(RHE\right)=E\left(Ag/AgCl\right)+0.059\times pH+0.222\,V$$

The cyclic voltammetry (CV) curves for the non-Faradaic regions were created, and the electric double layer capacitance (Cdl) was derived using the following equation:

$$C_{dl}=(j_a-j_c)/2$$

where (j_a-j_c) are the differences in the current density.

Product quantification

Here, 1.5 ml of cathodic reaction solution was obtained from the electrolytic cell each time, and the products were analyzed using HPLC with the detector set to 210 nm. The chromatographic column (Innoval ODS-2) was used at 30°C, and the sample was analyzed by a binary gradient method with a mobile phase containing 0.5% aqueous phosphoric acid and CH_3CN at a flow rate of 0.6 ml/min. The CH_3CN fraction was increased from an initial 15% (v/v) to 60% over a period of 5 to 15 min and then decreased to 15% over a period of 17 to 24 min. The products were

quantitatively analyzed by comparison with the standard curves established under the same conditions. The peaks of FA, furfural, and MF appeared at 6.5, 7.8, and 18.3 min, respectively. HFN (1,2-bis(furan-2-yl)ethane-1,2-diol) had two peak times, 8.6 and 12.5 min.

The selectivity, Faradaic efficiency (FE), and conversion of products were calculated by the following equations:

$$Selectivity(\%) = \frac{mole\ of\ \ product\ formed}{mole\ of\ \ initial\ \ substrate} \times 100\%$$

$$FE(\%) = \frac{mole\ of\ \ product\ formed}{total\ \ charge\ passed\ /\ (n \times F)} \times 100\%$$

$$Conversion(\%) = \frac{mole\ of\ \ product\ consumed}{mole\ of\ \ initial\ \ substrate} \times 100\%$$

The TOF (Turnover Frequency) is determined based on experimental data collected over a 2-hour period at a constant potential of 0.57 V vs. RHE. The activity of copper foam was simultaneously subtracted. The calculation follows the formula[3].

$$TOF = \frac{I_{total} \times FE}{N \times F \times n_{catalyst}}$$

Where Itotal is the total current, N represents the number of electrons transferred in the reduction of furfural to furfuryl alcohol (N = 2), F is the Faraday constant, and ncatalyst is the moles of the catalyst coated on the electrode (mol).

Computational models and methods

Five catalyst models were employed in this study. The initial structures of $[Ag_{17}Cu_{12}]^{3-}$, $[Ag_{29}]^{3-}$, and $[AuAg_{16}Cu_{12}]^{3-}$, were taken directly from their crystallographic data, while the $[Ag_{17}Cu_{12}]^{2-*}$ and $[Cu_{29}]^{3-}$ models were constructed based on the $[Ag_{17}Cu_{12}]^{3-}$ framework. All structures were

optimized using the Dmol[3] package at the BP/DND level with the effective core potential (ECP) pseudopotential[4-6]. The convergence tolerances of energy, force, and displacement for structure relaxation were 2.0×10^{-5} Ha, 4.0×10^{-3} Ha/Å, and 5.0×10^{-3} Å, respectively. Notably, the structure of $[Ag_{17}Cu_{12}]^{2-*}$ was almost the same as that of $[Ag_{17}Cu_{12}]^{3-}$. Based on the optimized structures, the conductor-like screening model (COSMO)[7, 8] was employed for aqueous-phase single-point calculations with consideration of the solvent (water).

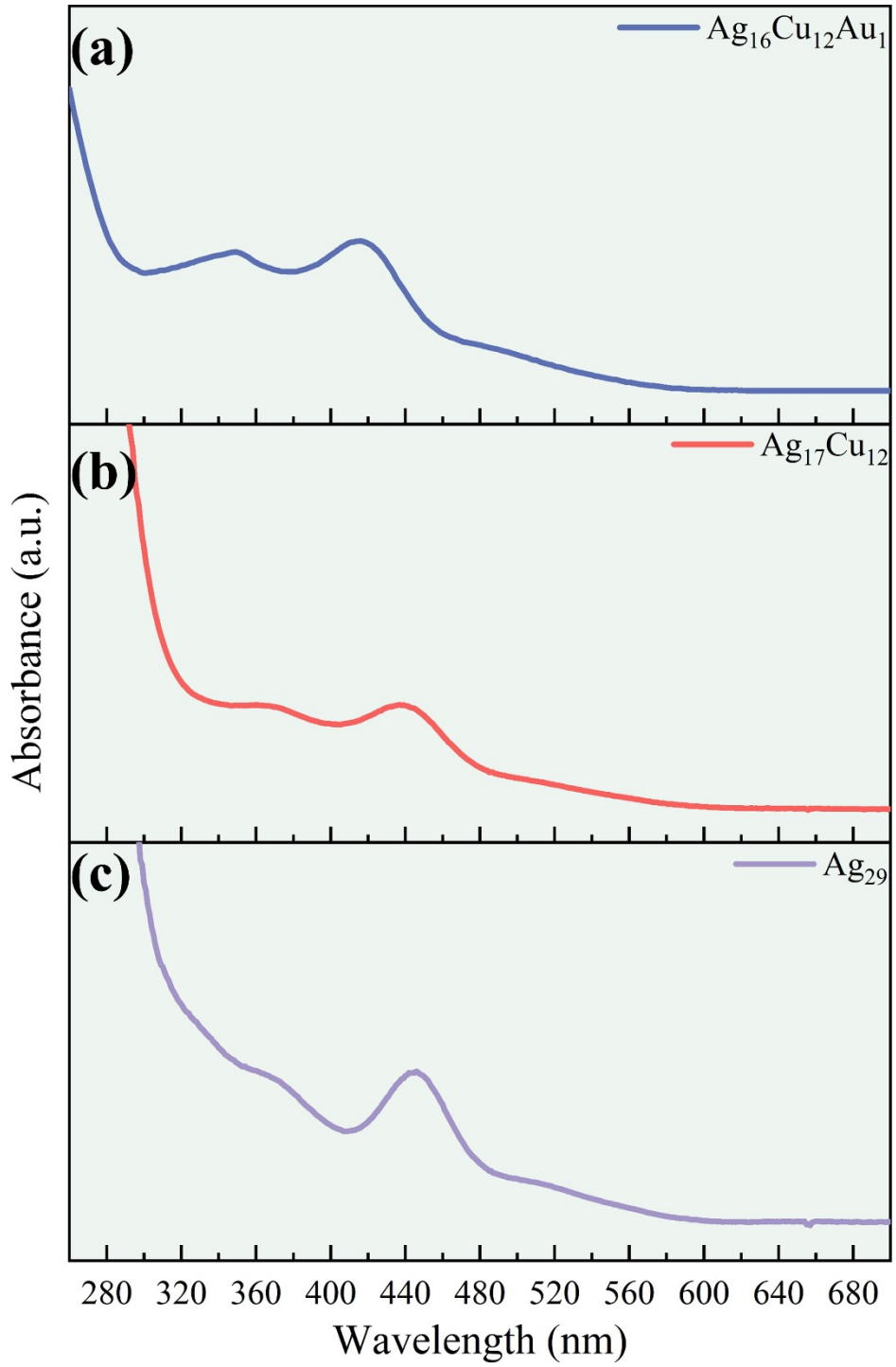

Figure S1. Ultraviolet–visible (UV–vis) absorbance spectrum of the $Ag_{16}Cu_{12}Au_1$, $Ag_{17}Cu_{12}$, and Ag_{29} nanoclusters.

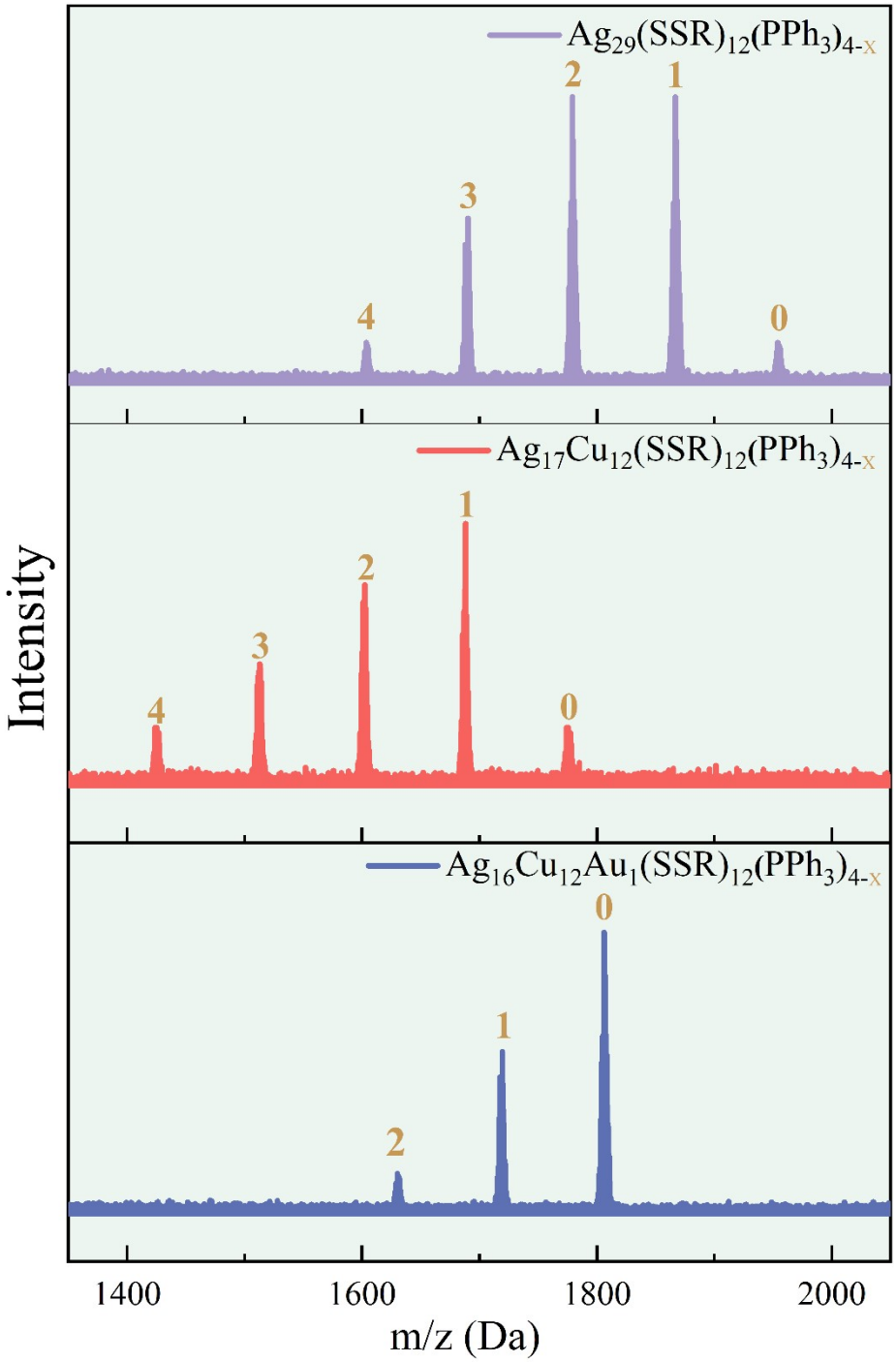

Figure S2. ESI-TOF-MS results of the Ag_{29}, $Ag_{17}Cu_{12}$, and $Ag_{16}Cu_{12}Au_1$ nanoclusters.

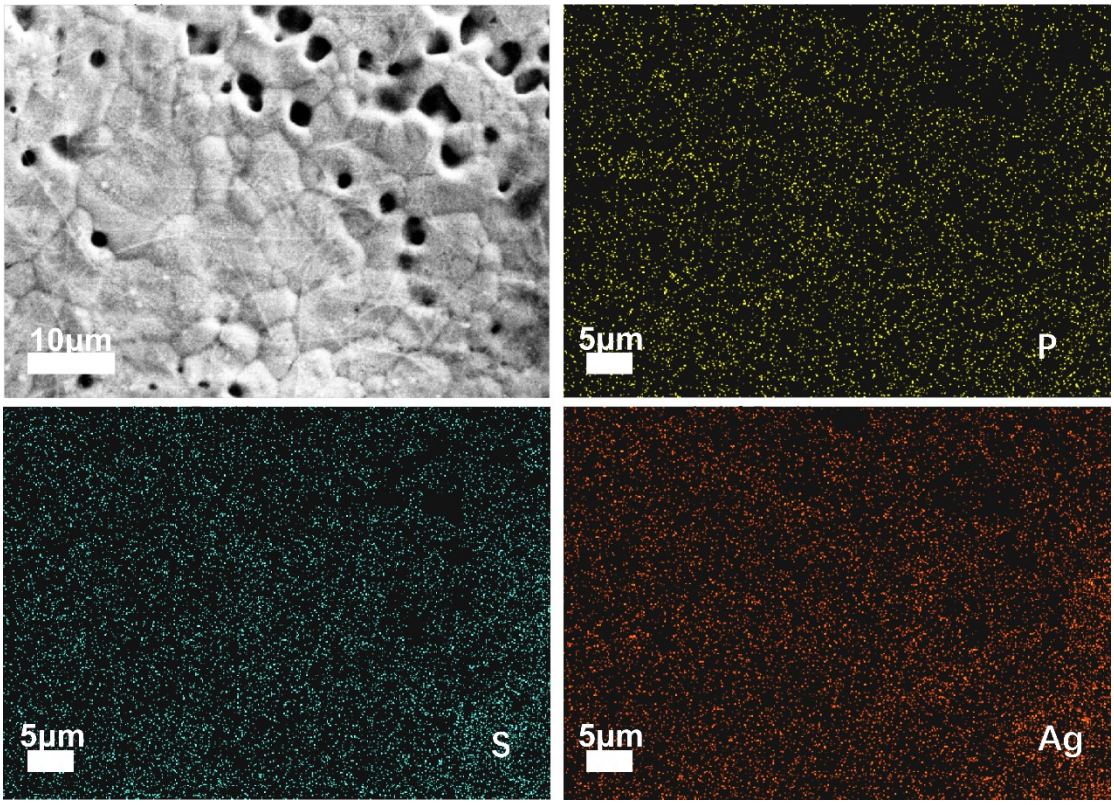

Figure S3. SEM and EDS mapping images of Ag_{29}/CuF.

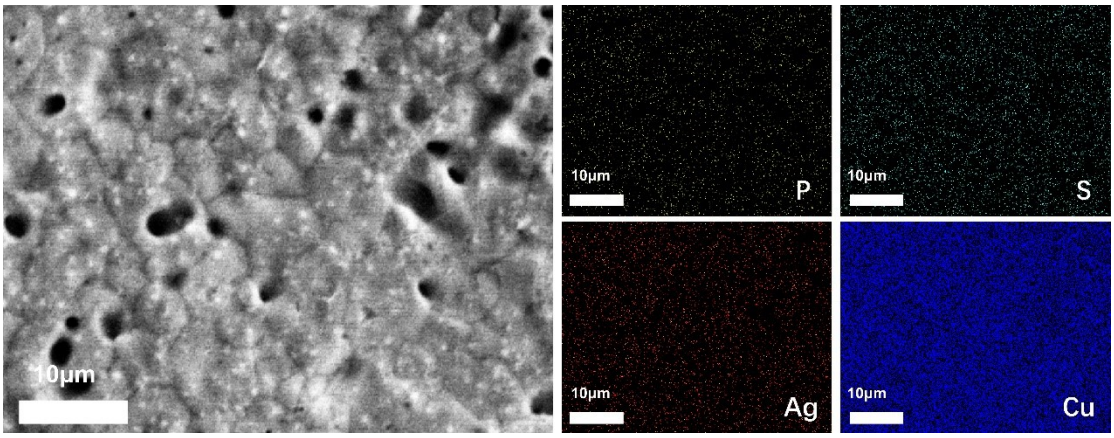

Figure S4. SEM and EDS mapping images of $Ag_{17}Cu_{12}$/CuF.

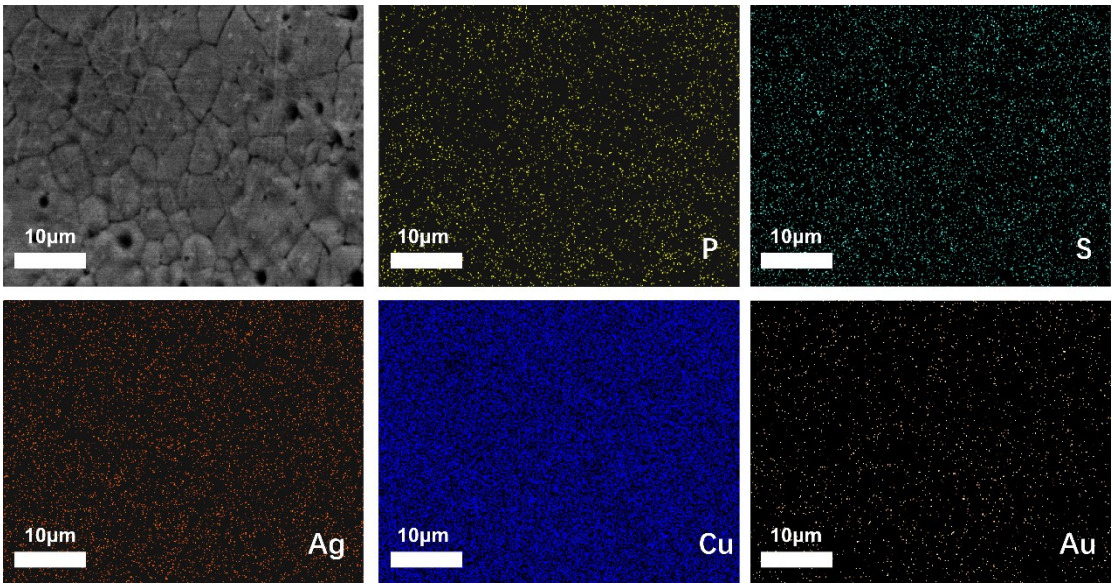

Figure S5. SEM and EDS mapping images of $Ag_{16}Cu_{12}Au_1$/CuF.

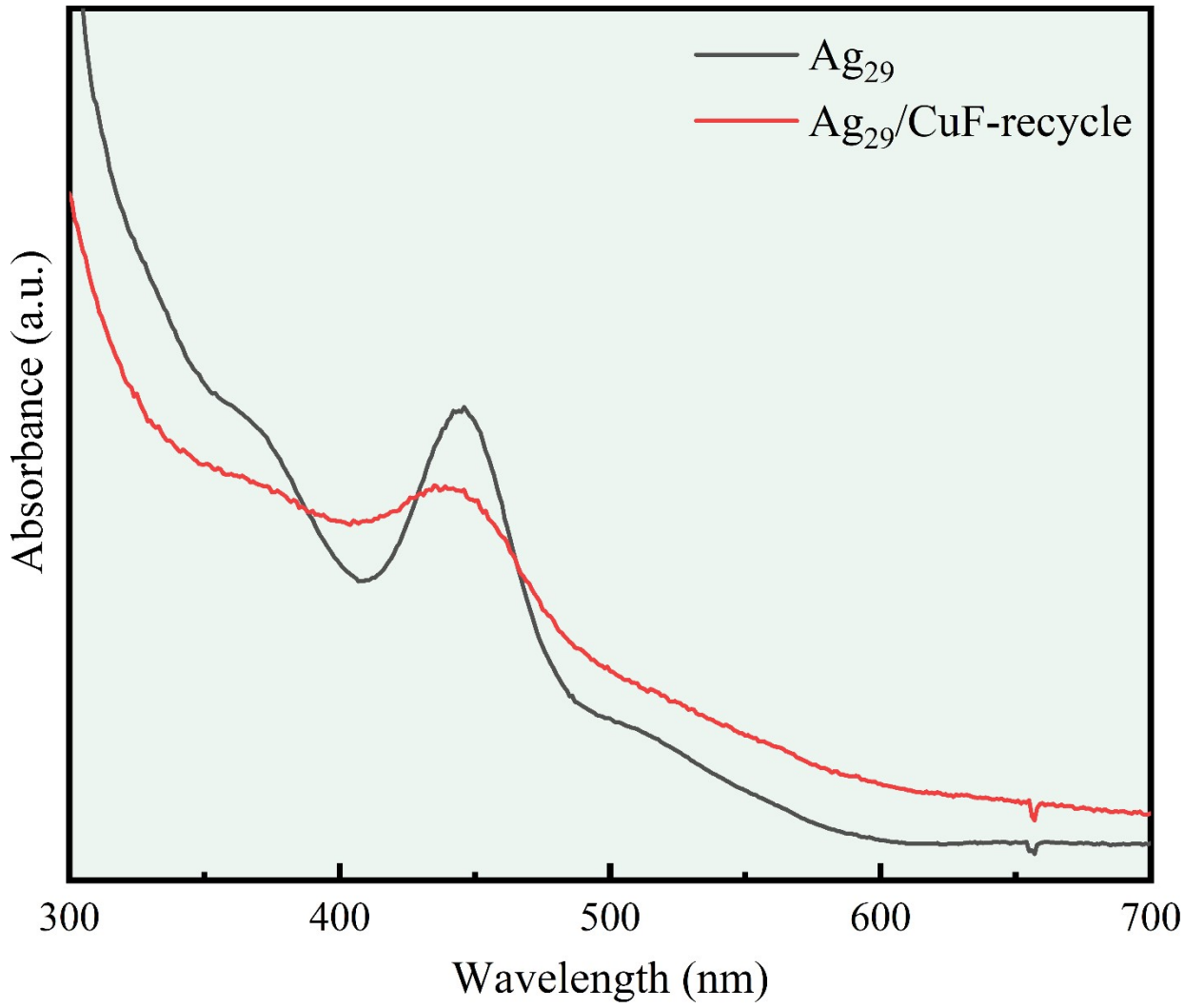

Figure S6. Ultraviolet-visible (UV-vis) absorbance spectra of the Ag_{29} and recycled Ag_{29} nanoclusters.

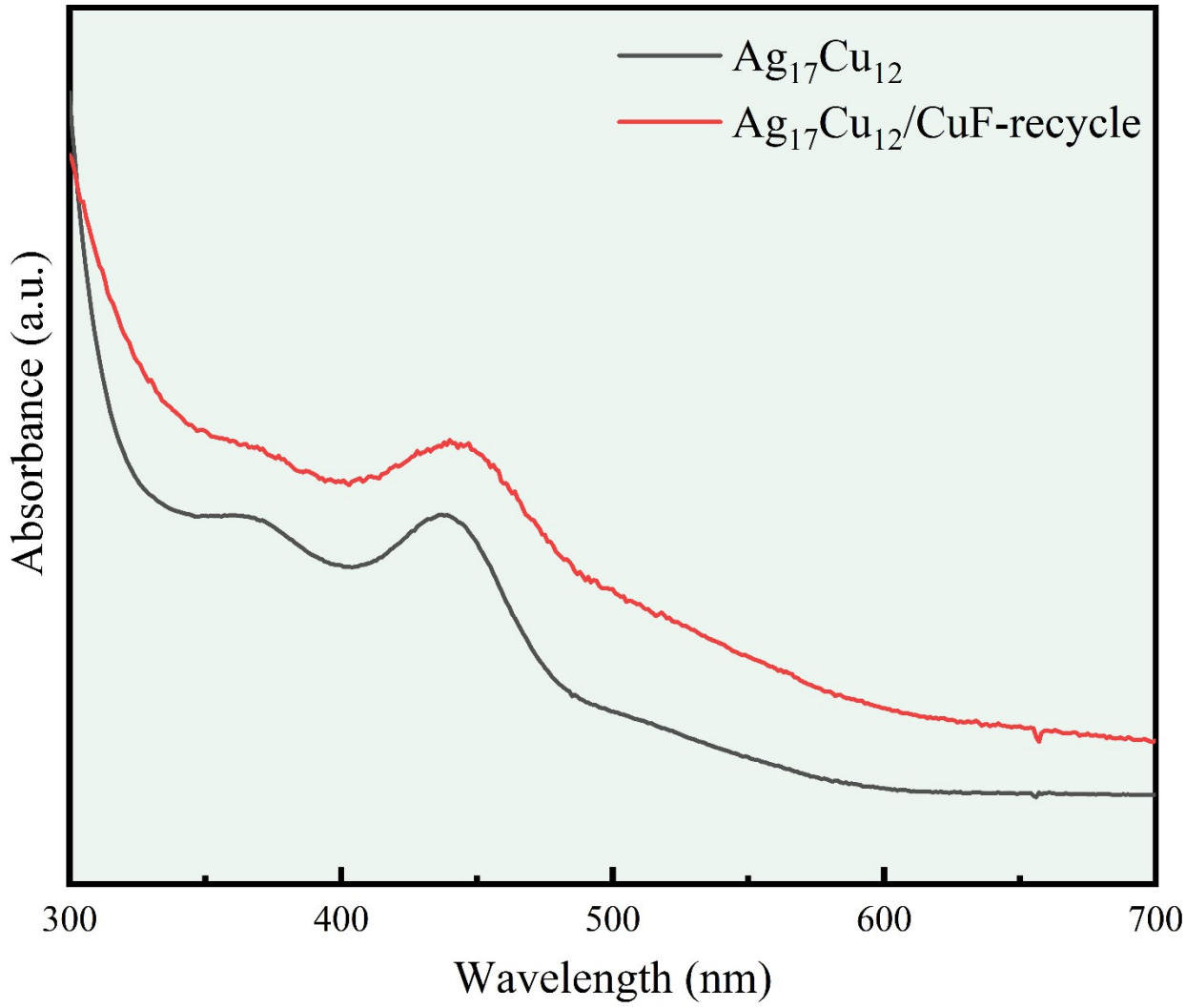

Figure S7. Ultraviolet-visible (UV-vis) absorbance spectra of the $Ag_{17}Cu_{12}$ and recycled $Ag_{17}Cu_{12}$ nanoclusters.

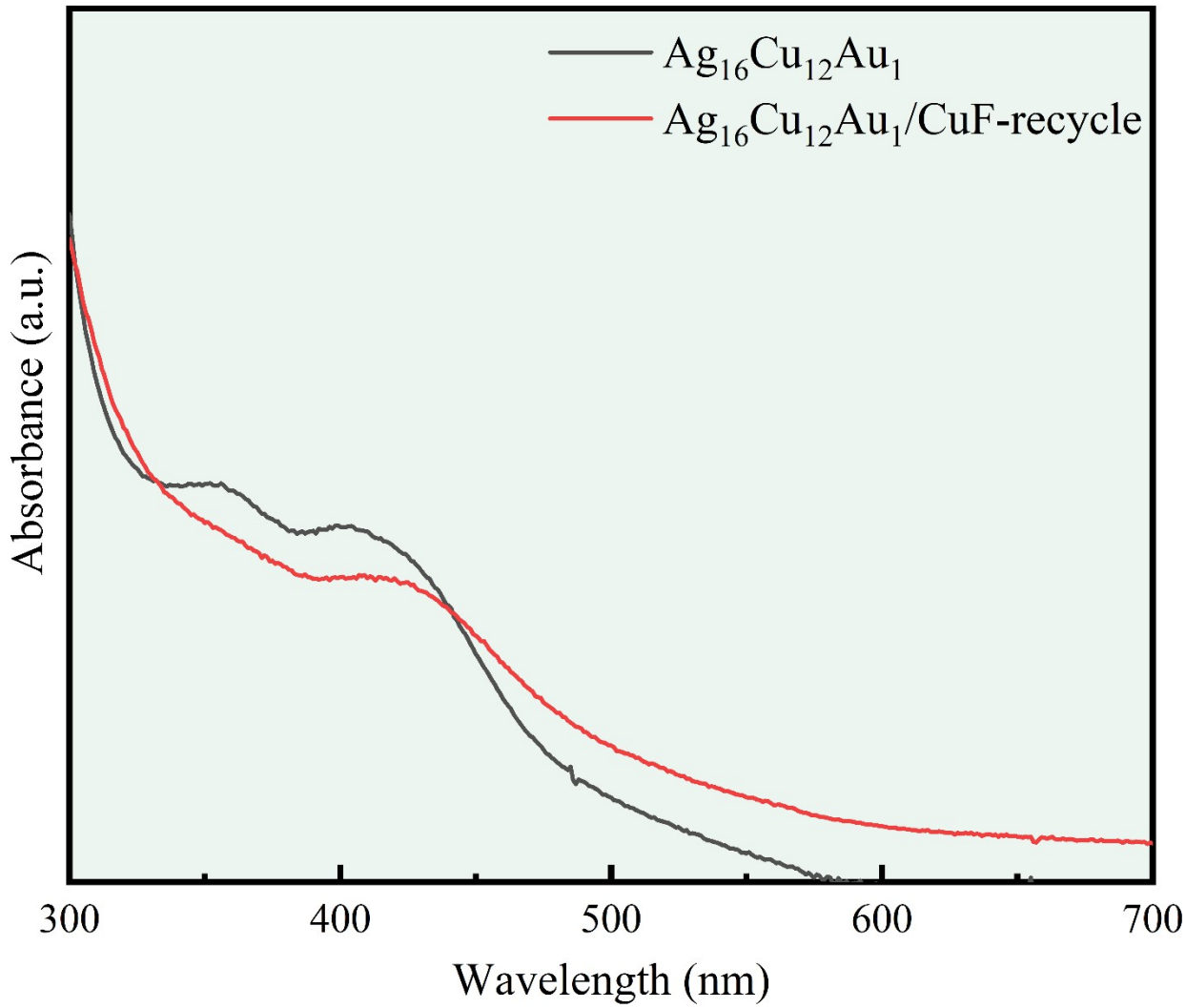

Figure S8. Ultraviolet-visible (UV-vis) absorbance spectra of the $Ag_{16}Cu_{12}Au_1$ and recycled $Ag_{16}Cu_{12}Au_1$ nanoclusters.

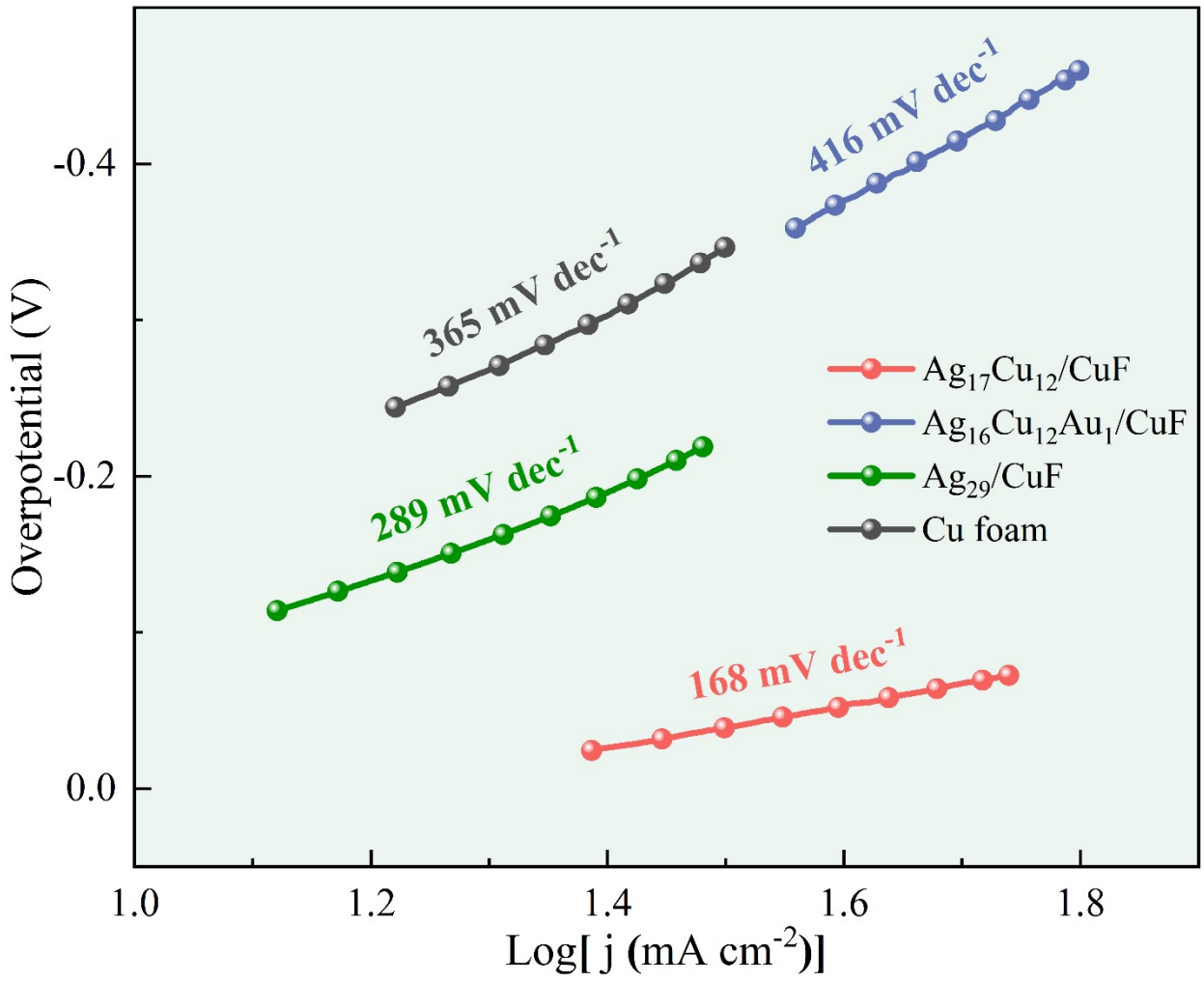

Figure S9. Corresponding Tafel slopes of different nanoclusters loaded on Cu foam in 0.5 M K_2SO_4 electrolyte without furfural.

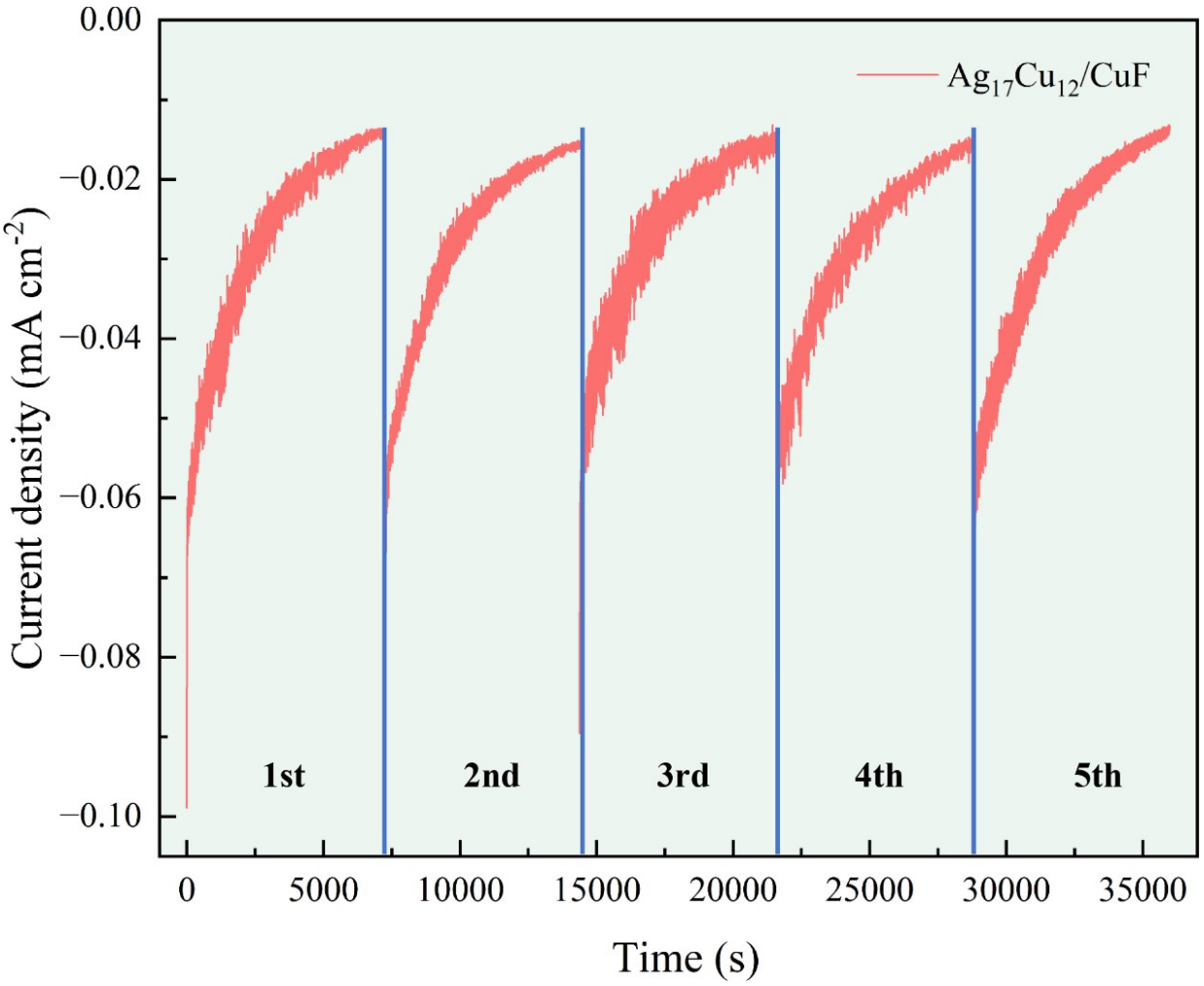

Figure S10. Current–time (i-t) profiles of $Ag_{17}Cu_{12}$/CuF during five durability cycles at -0.57 V vs. RHE.

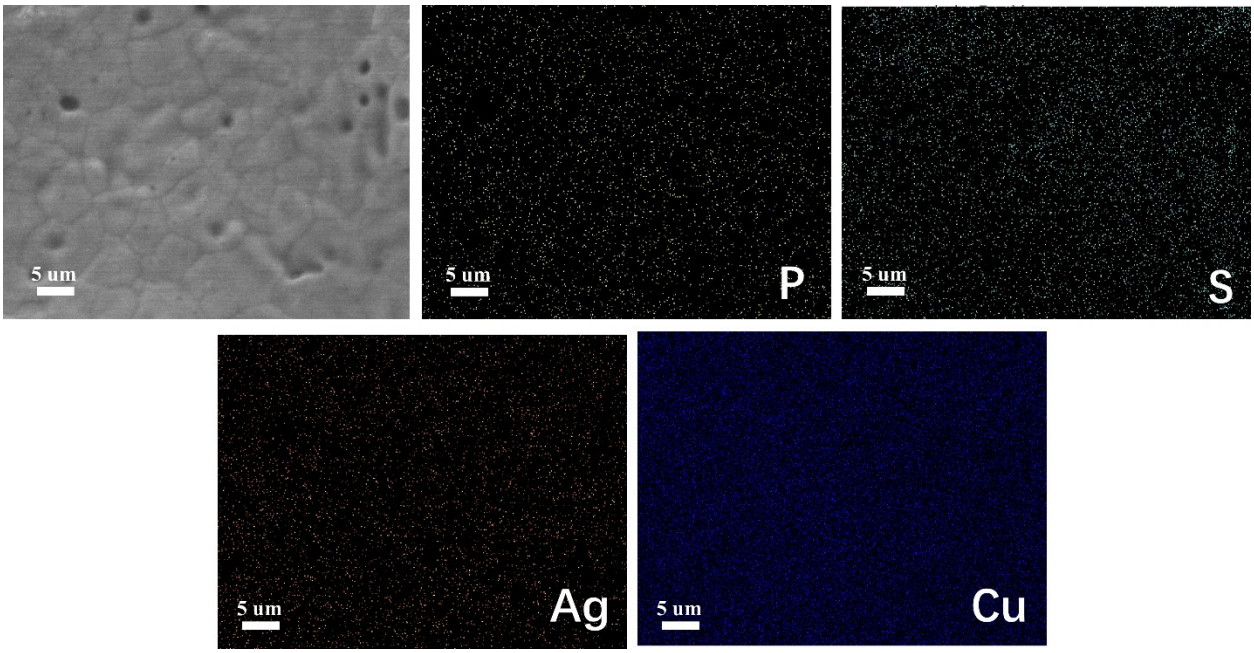

Figure S11. SEM and EDS mapping images of $Ag_{17}Cu_{12}$/CuF after five cycles.

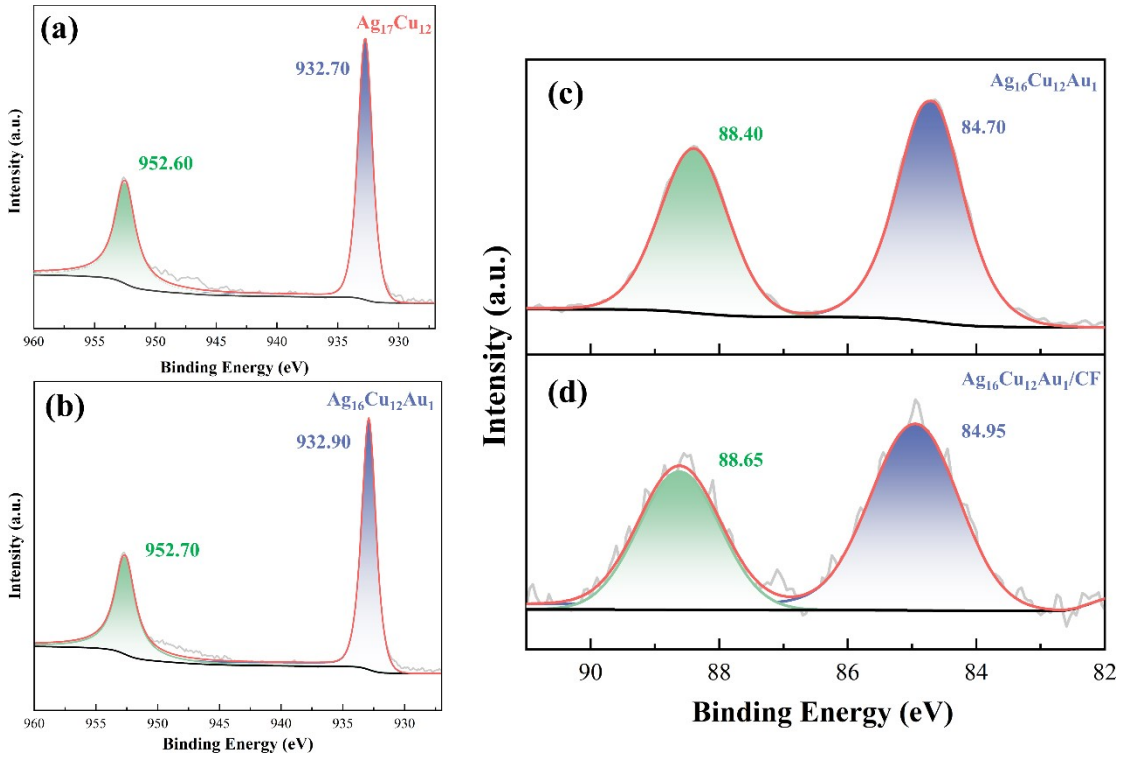

Figure S12. XPS spectra of the different catalysts for Cu 2p and Au 4f orbitals. (a) Cu 2p spectra of $Ag_{17}Cu_{12}$. (b) Cu 2p spectra of $Ag_{16}Cu_{12}Au_1$. (c) Au 4f spectra of $Ag_{16}Cu_{12}Au_1$. (d) Au 4f spectra of $Ag_{16}Cu_{12}Au_1$ loaded on copper foam.

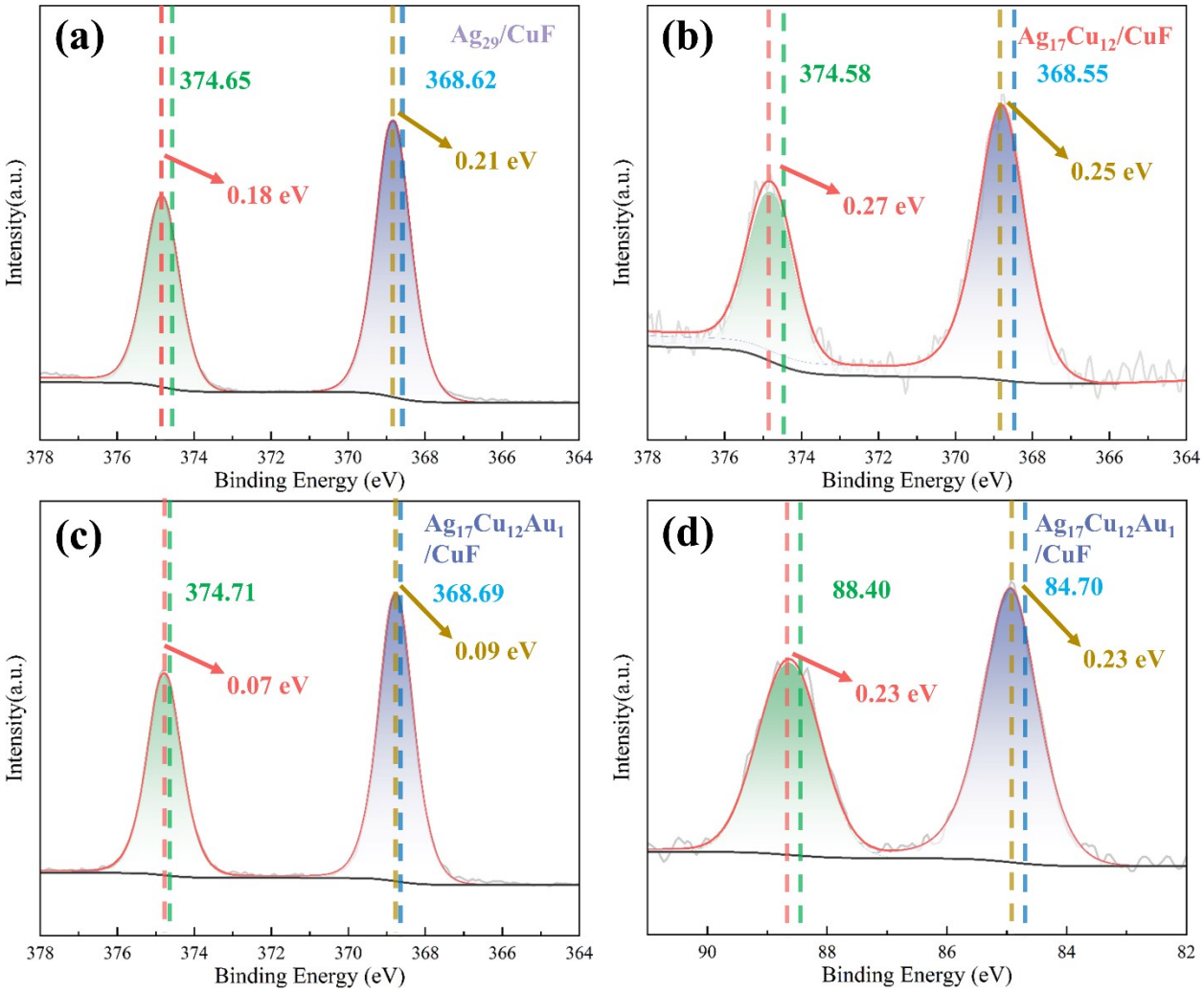

Figure S13. XPS spectra of the post-reaction catalysts for Ag 3d and Au 4f orbitals. (a) Ag 3d spectra of Ag_{29}/CuF. (b) Ag 3d spectra of $Ag_{17}Cu_{12}$/CuF. (c) Ag 3d spectra of $Ag_{17}Cu_{12}Au_1$/CuF. (d) Au 4f spectra of $Ag_{17}Cu_{12}Au_1$/CuF. The green and blue lines represent the positions of the peaks of the original nanoclusters, and the pink and yellow lines represent the corresponding peak positions after the electrocatalytic reaction.

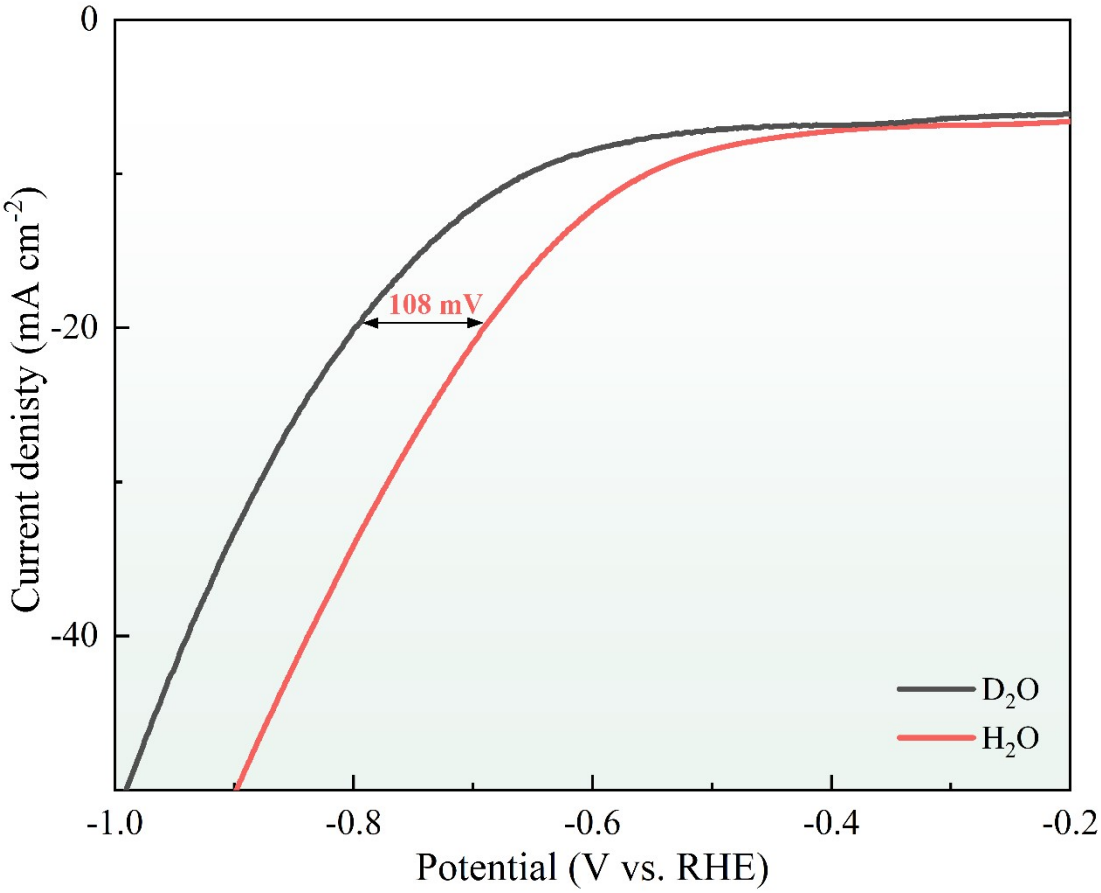

Figure S14. Comparison of the LSV curves of $Ag_{17}Cu_{12}$/CuF in 0.5 M K_2SO_4 aqueous solution and deuterium aqueous solution without furfural.

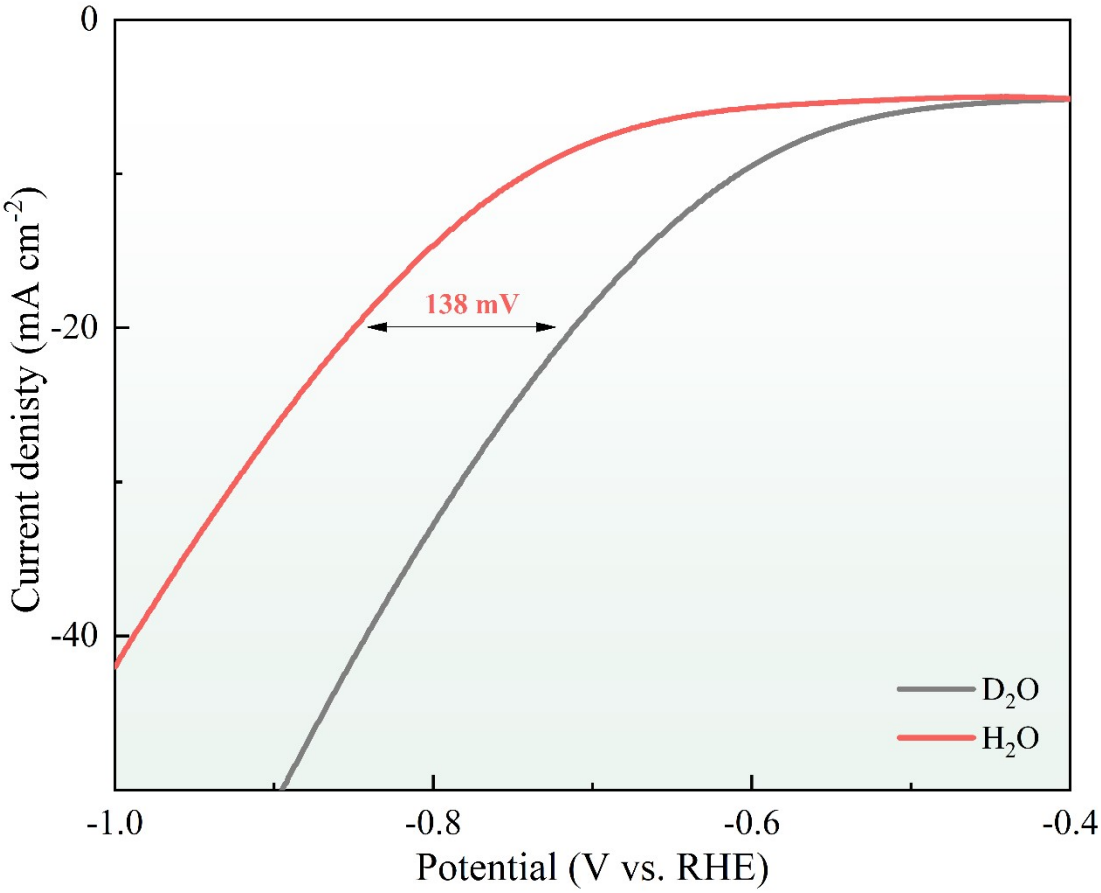

Figure S15. Comparison of the LSV curves of Cu foam in 0.5 M K_2SO_4 aqueous solution and deuterium aqueous solution without furfural.

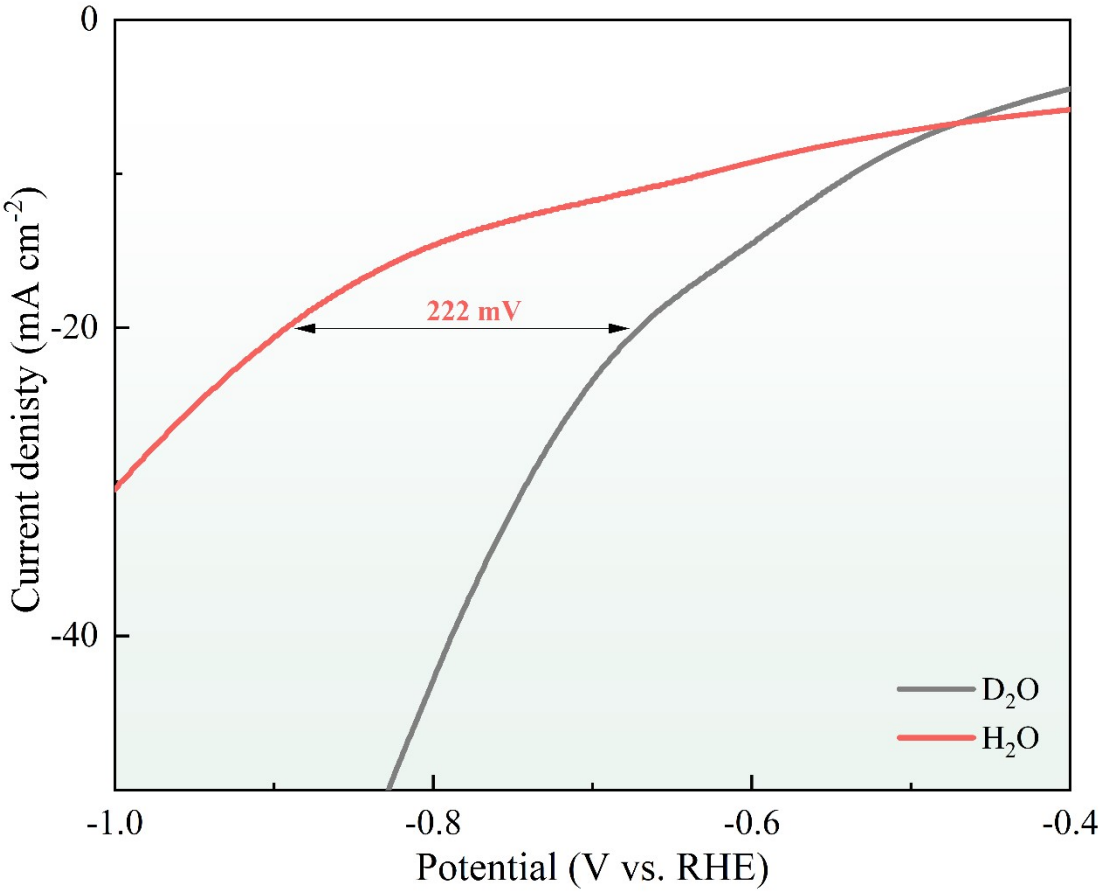

Figure S16. Comparison of the LSV curves of Cu foam in 0.5 M K_2SO_4 aqueous solution and deuterium aqueous solution with the addition of 20 mM furfural.

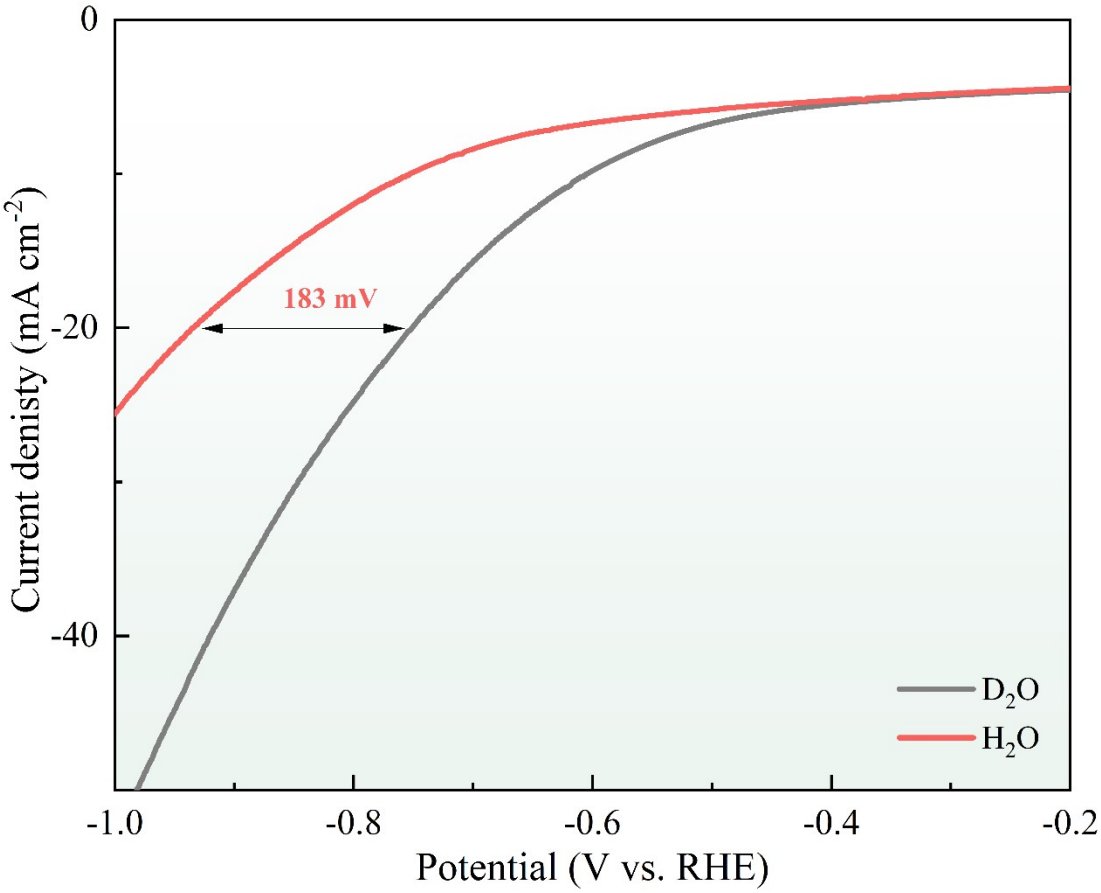

Figure S17. Comparison of the LSV curves of Ag_{29}/CuF in 0.5 M K_2SO_4 aqueous solution and deuterium aqueous solution without furfural.

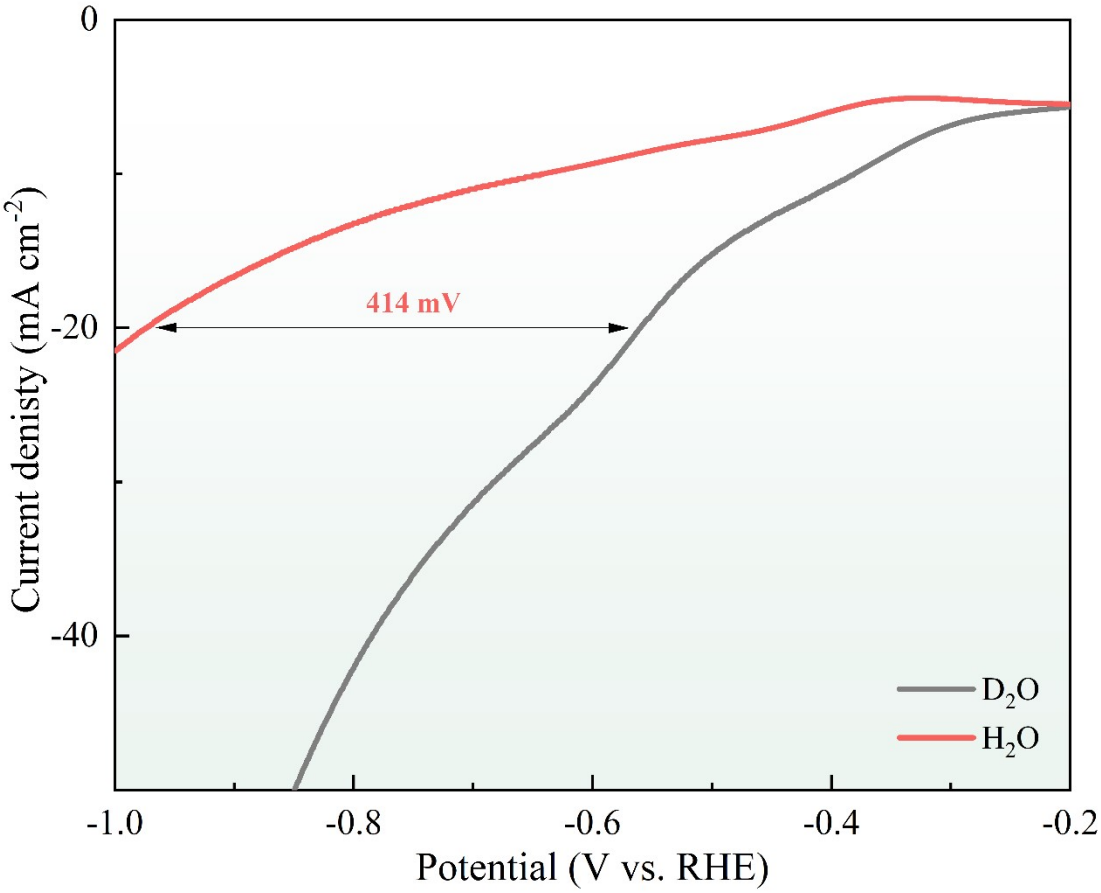

Figure S18. Comparison of the LSV curves of Ag_{29}/CuF in 0.5 M K_2SO_4 aqueous solution and deuterium aqueous solution with the addition of 20 mM furfural.

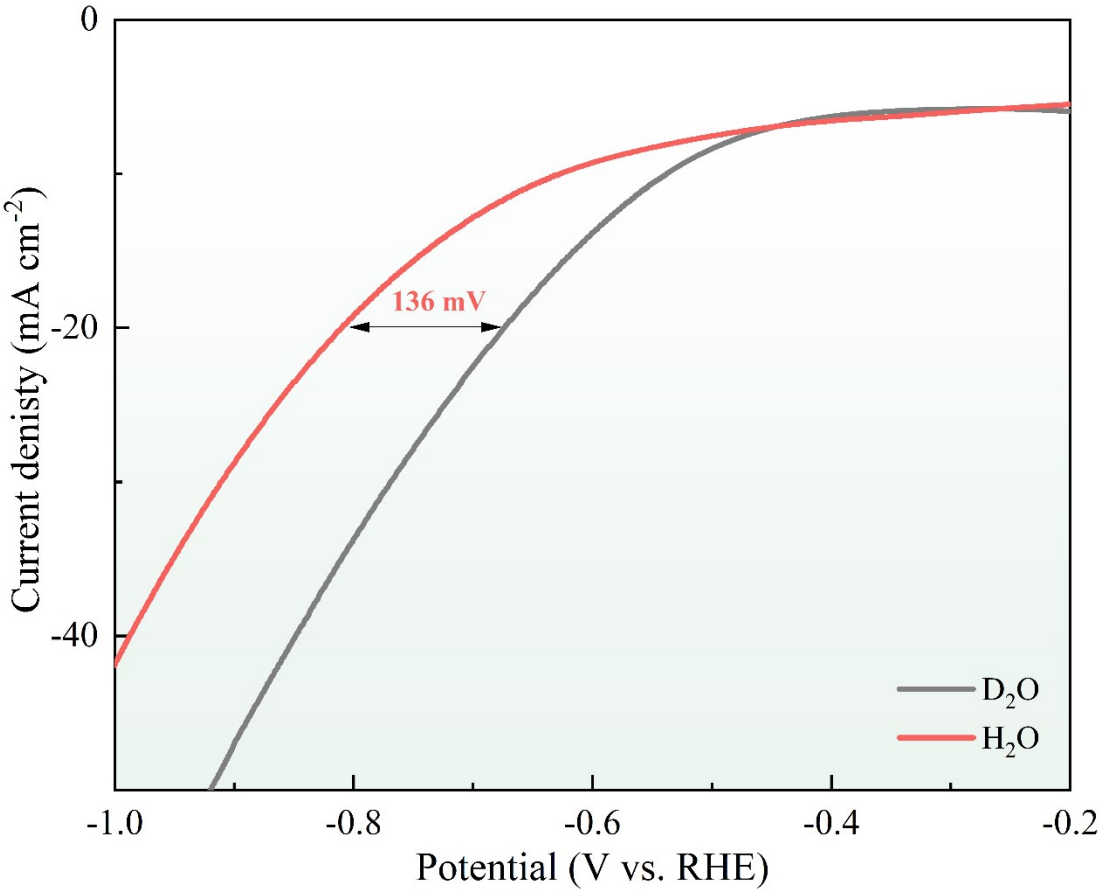

Figure S19. Comparison of the LSV curves of $Ag_{16}Cu_{12}Au_1$/CuF in 0.5 M K_2SO_4 aqueous solution and deuterium aqueous solution without furfural.

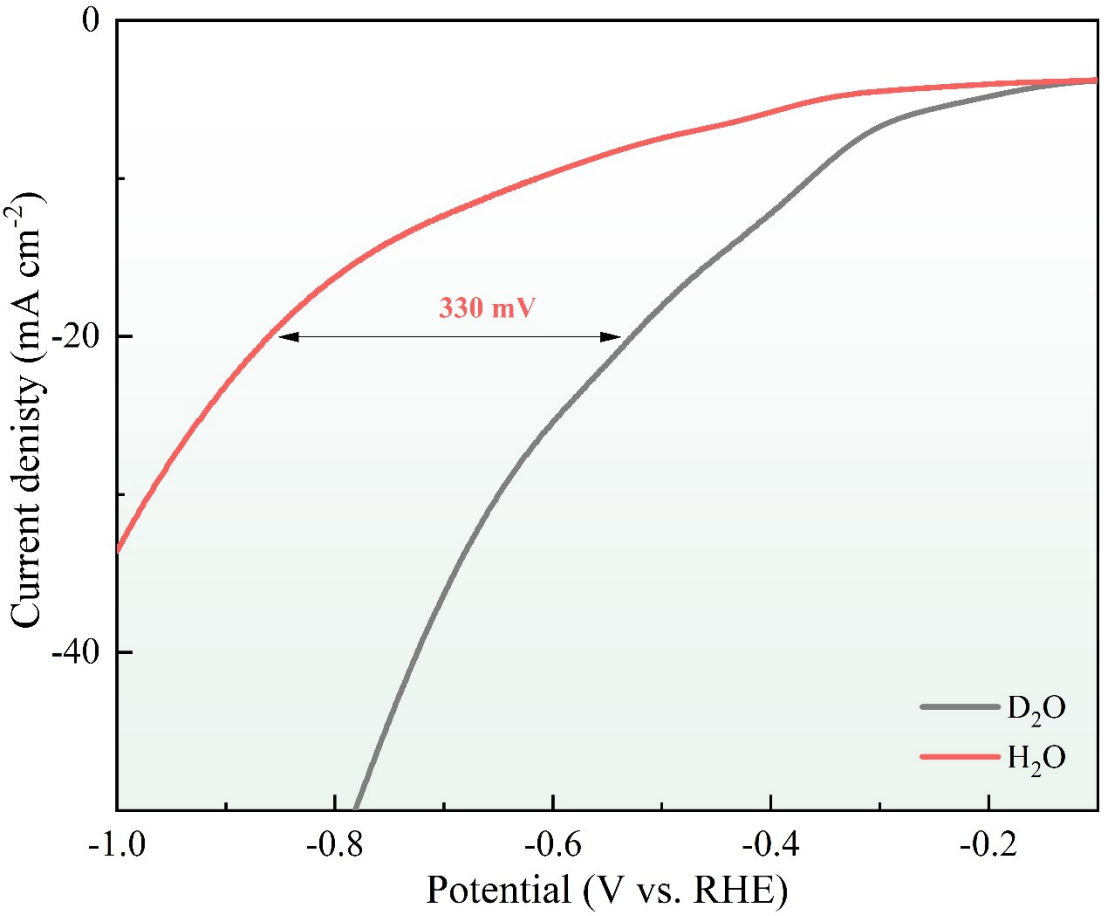

Figure S20. Comparison of the LSV curves of $Ag_{16}Cu_{12}Au_1$/CuF in 0.5 M K_2SO_4 aqueous solution and deuterium aqueous solution with the addition of 20 mM furfural.

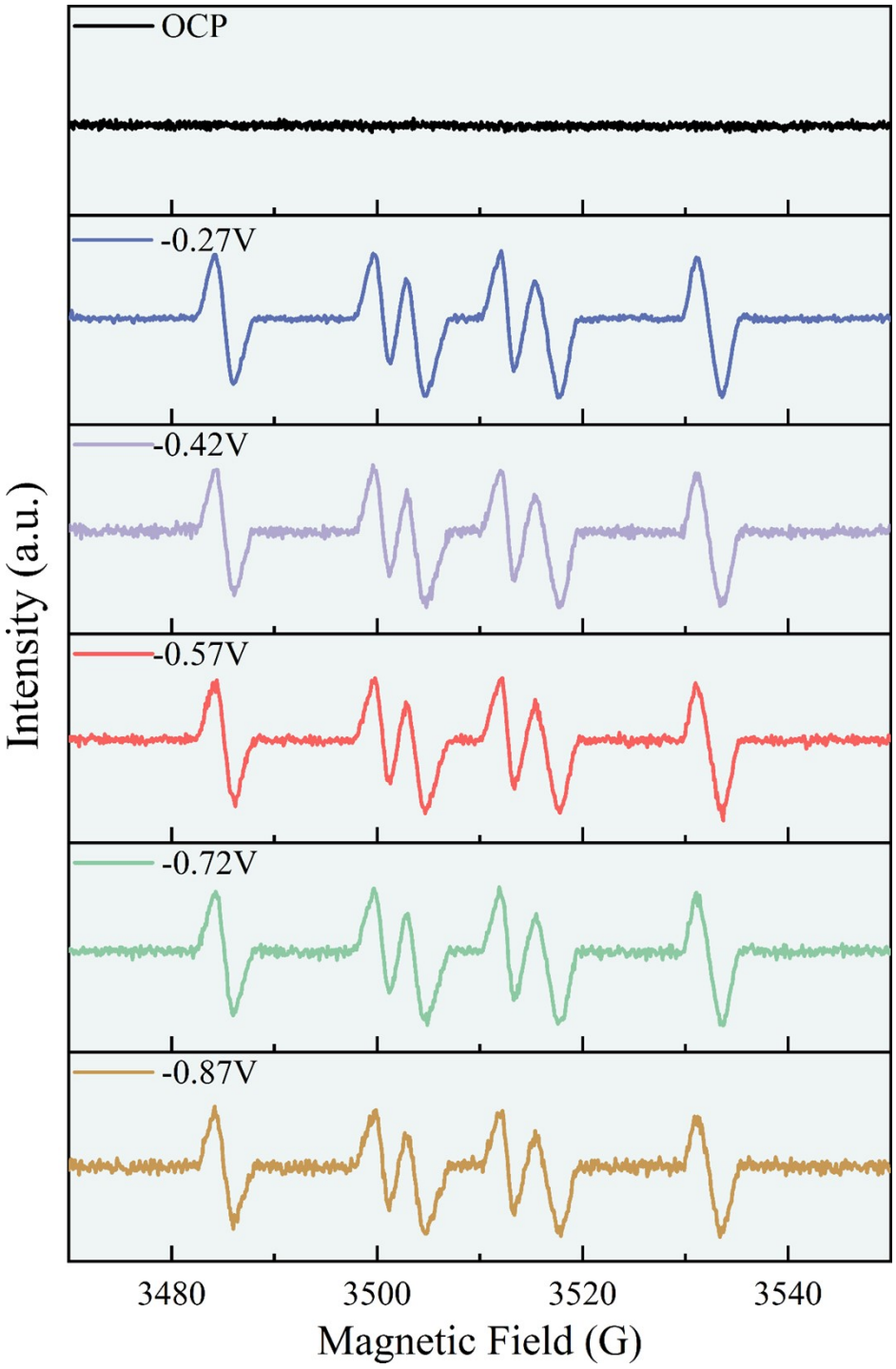

Figure S21. In situ EPR trapping of the carbon radicals over $Ag_{17}Cu_{12}$/CuF.

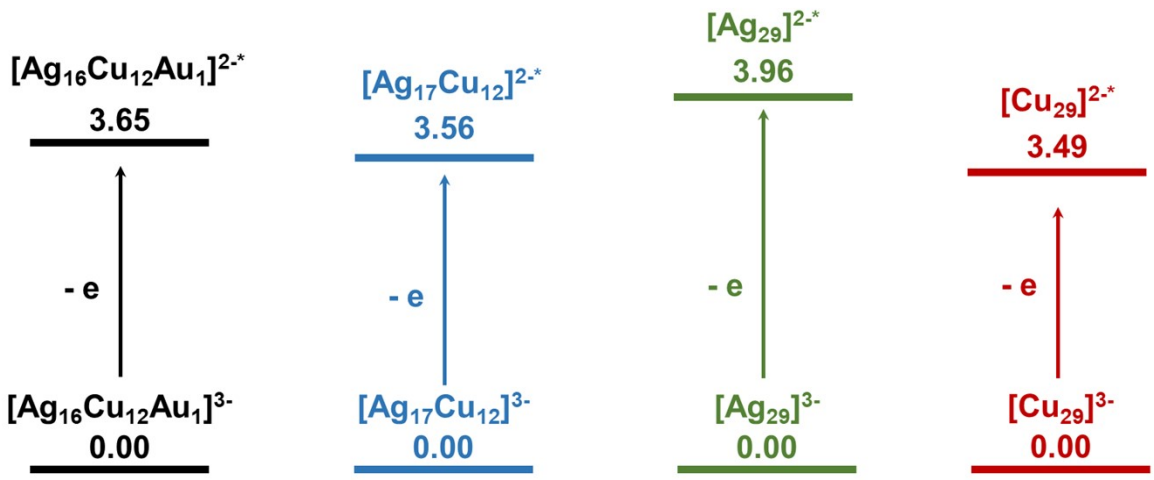

Figure S22. Electron transfer capabilities of $[Ag_{17}Cu_{12}]^{3-}$, $[Ag_{29}]^{3-}$, $[Cu_{29}]^{3-}$, and $[Ag_{16}Cu_{12}Au_1]^{3-}$

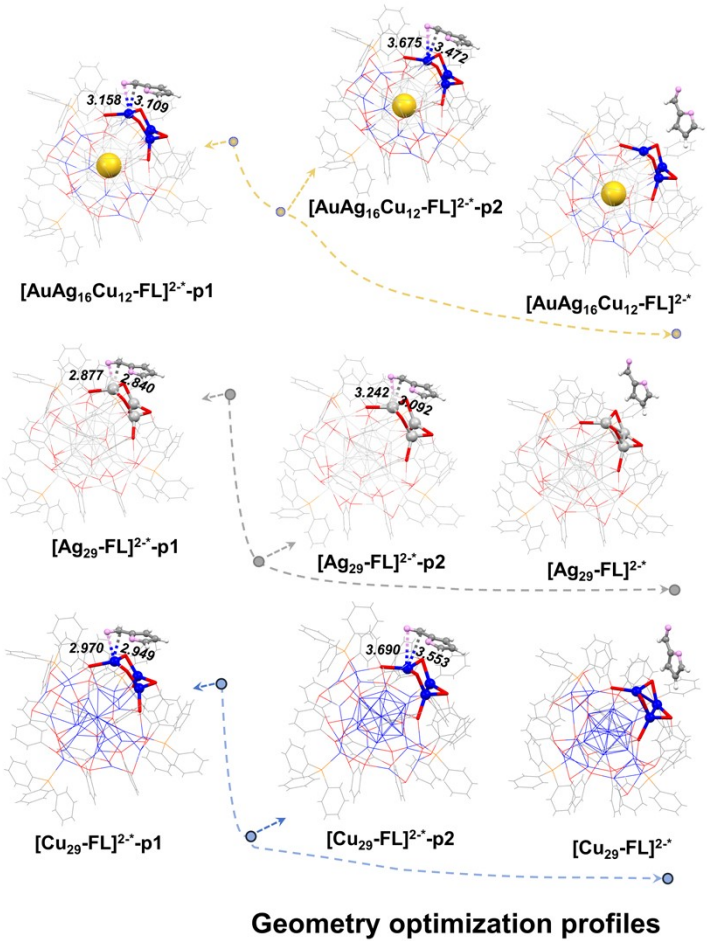

Figure S23. The optimization profiles of $[AuAg_{16}Cu_{12}\text{-}FL]^{2-*}$, $[Ag_{29}\text{-}FL]^{2-*}$, and $[Cu_{29}\text{-}FL]^{2-*}$.

Table S1. Comparison of $Ag_{17}Cu_{12}$/CuF with the current studies for the electrocatalytic hydrogenation (ECH) reaction of furfural.

Catalyst	Electrolyte	Time (h)	Potential (vs. RHE)	Current Density (mA/cm²)	Furfural (mM)	Temp (°C)	Loading (mg/cm²)	TOF (h^{-1})	Ref.
MoS_2	0.4M sodium borate buffer	-	-0.47 V	-	20	25	0.036	917	9
15%-Cu/NC_{900}	1.0 M KOH solution	4	-0.25 V	-	30	25	3.0	52	10
CuO/RuO_2/C	1.0 M KOH solution	2	-0.274 V	-	50	25	2.0	109	11
CuO/C	1.0 M KOH solution	2	-0.274 V	-	50	25	2.0	149	
Cu/C	sodium acetate-acetic acid buffer (pH 5.2)	2	-0.50 V	-	20	25	2.2	320	12
Rh/C	sodium acetate-acetic acid buffer (pH 5.2)	2	-0.10 V	-	20	25	2.2	104	
Ru/C	sodium acetate-acetic acid buffer (pH 5.2)	2	-0.10 V	-	20	25	2.2	100	
Pd/C	sodium acetate-acetic acid buffer (pH 5.2)	1	-0.10 V	-	20	25	2.2	64	
Rh/C	acetate buffer (pH 4.6; 3M sodium acetate and acetic acid)	2	-0.43 V	-	20	25	2.22	750	13
MoS_2/CFC	0.1M phosphate buffer	5	-0.80 V	-	12.5	25	0.56	13	14
CoPc/MWCNT	0.1M Carbonate buffer	1	-0.50 V	-	8	25	0.1	1440	15
CuPc/ MWCNT	0.1M Carbonate buffer	1	-0.50 V	-	8	25	0.1	1260	
TAP 900@Cr	0.1M Carbonate buffer	1	-0.50 V	-	8	25	0.1	954	16
Pd/C	47.5wt.% isopropanol, 47.5wt.%	-	-0.8 V	-	80	25	0.25	315	17

	H2O,5 wt.% acetic acid								
Ru/C	47.5wt.% isopropanol, 47.5wt.% H_2O,5 wt.% acetic acid	-	-0.8 V	-	80	25	0.24	150	
Ni/C	47.5wt.% isopropanol, 47.5wt.% H_2O,5 wt.% acetic acid	-	-0.8 V	-	80	25	0.14	155	
Cu/C	47.5wt.% isopropanol, 47.5wt.% H_2O,5 wt.% acetic acid	-	-0.8 V	-	80	25	0.15	110	
Co/C	47.5wt.% isopropanol, 47.5wt.% H_2O,5 wt.% acetic acid	-	-0.8 V	-	80	25	0.16	90	
Rh/C	47.5wt.% isopropanol, 47.5wt.% H_2O,5 wt.% acetic acid	-	-0.8 V	-	80	25	0.24	30	
CuO_{1-x}/CF	0.2 M PBS	1	-	-20	20	25	-	43	[18]
Cu/NC	0.1M acetate buffer	0.5	-	-5.1	40	25	1	46	[19]
Cu/OC	0.1M Na_2SO_4 solution	2	-0.6 V	-	100	25	1	2916	[20]
Cu-MoS_2/CC	0.1M phosphate buffer/MeOH	4	-0.6 V	-	20	25	0.0006	3582	[21]
$Cu_{1.15}/P_{Ag}$	1 M KOH solution	3	-0.28 V	-	10	25	-	114	[22]
Ag_{29}/CuF	**0.5 M K_2SO_4 solution**	**2**	**-0.57 V**	**-**	**20**	**25**	**0.5**	**543.8**	
$Ag_{16}Cu_{12}Au_1$/CuF	**0.5 M K_2SO_4 solution**	**2**	**-0.57 V**	**-**	**20**	**25**	**0.5**	**1595.2**	**This work**
$Ag_{17}Cu_{12}$/CuF	**0.5 M K_2SO_4 solution**	**2**	**-0.57 V**	**-**	**20**	**25**	**0.5**	**3752.4**	

Table S2. Comparison of the electrocatalytic performance of $Ag_{17}Cu_{12}$/CuF in acidic, alkaline, and neutral electrolytes.

Catalyst	Electrolyte	Time (h)	Furfural (mM)	Loading (mg/cm²)	Potential (vs. RHE)	FE of furfural	Selectivity of furfural	Conversion rate
$Ag_{17}Cu_{12}$/CuF	0.5 M K_2SO_4	2	20	5	-0.57 V	67.4%	71.6%	100%
$Ag_{17}Cu_{12}$/CuF	0.1 M KOH	2	20	5	-0.57 V	53.4%	49.3%	45.1%
$Ag_{17}Cu_{12}$/CuF	phosphate-acetate buffer, pH 3.0	2	20	5	-0.57 V	5.0%	37.1%	70.1%

Table S3. Concentrations of Ag, Cu, and Au in the electrolyte after electrolysis and the corresponding leaching rates.

Sample	Ag(μg/L)	Cu(μg/L)	Au(μg/L)	Leaching rate*
Ag_{29}/CuF	11.49	22.44	\	0.037%
$Au_1Ag_{16}Cu_{12}$/CuF	1.40	4.41	1.69	0.086%
$Ag_{17}Cu_{12}$/CuF	7.16	14.55	\	0.039%

*The leaching rates of all nanoclusters were determined based on Ag as the reference.

References

1. S. Liu, Z. Mukadam, S. B. Scott, S. C. Sarma, M. M. Titirici, K. Chan, N. Govindarajan, I. E. L. Stephens and G. Kastlunger, *EES Catalysis*, 2023, **1**, 539-551.
2. X. Kang, H. Abroshan, S. Wang and M. Zhu, *Inorganic Chemistry*, 2019, **58**, 11000-11009.
3. J. Zhao, A. Ziarati, A. Rosspeintner and T. Burgi, *Angewandte Chemie International Edition*, 2024, **63**, e202316649.
4. B. Delley, *The Journal of Chemical Physics*, 1990, **92**, 508-517.
5. B. Delley, *The Journal of Physical Chemistry*, 1996, **100**, 6107-6110.
6. B. Delley, *The Journal of Chemical Physics*, 2000, **113**, 7756-7764.
7. A. Klamt and G. Schüürmann, *Journal of the Chemical Society, Perkin Transactions 2*, 1993, 799-805.
8. J. Tomasi and M. Persico, *Chemical Reviews*, 2002, **94**, 2027-2094.
9. S. Q. Huang, B. Gong, Y. X. Jin, P. H. L. Sit and J. C. H. Lam, *Acs Catalysis*, 2022, **12**, 11340-11354.
10. W. L. Xu, C. J. Yu, J. Z. Chen and Z. Y. Liu, *Applied Catalysis B-Environment and Energy*, 2022, **305**, 121062.
11. S. S. Naik, J. Theerthagiri, A. H. Min, C. J. Moon, S. J. Lee and M. Y. Choi, *Applied Catalysis B-Environment and Energy*, 2023, **339**, 123164.
12. U. Sanyal, K. Koh, L. C. Meyer, A. Karkamkar and O. Y. Gutiérrez, *Journal of Applied Electrochemistry*, 2020, **51**, 27-36.
13. U. Sanyal, J. Lopez-Ruiz, A. B. Padmaperuma, J. Holladay and O. Y. Gutiérrez, *Organic Process Research and Development*, 2018, **22**, 1590-1598.
14. T. Wu and M. Han, *Materials Advances*, 2022, **3**, 8250-8259.
15. Z. Mukadam, S. H. Liu, A. Pedersen, J. Barrio, S. Fearn, S. C. Sarma, M. M. Titirici, S. B. Scott, I. E. L. Stephens, K. R. Chan and S. Mezzavilla, *Energy & Environmental Science*, 2023, **16**, 2934-2944.
16. S. H. Liu, Z. Mukadam, A. Pedersen, J. Barrio, J. Parker, H. Tyrrell, S. J. Haigh, M. M. Titirici, I. E. L. Stephens and G. Kastlunger, *Journal of Physical Chemistry C*, 2025, **129**, 5032-5042.
17. J. A. Lopez-Ruiz, E. Andrews, S. A. Akhade, M. S. Lee, K. Koh, U. Sanyal, S. F. Yuk, A. J. Karkamkar, M. A. Derewinski, J. Holladay, V. A. Glezakou, R. Rousseau, O. Y. Gutiérrez and J. D. Holladay, *Acs Catalysis*, 2019, **9**, 9964-9972.
18. S. Guo, J. Ren, J. Chang, Y. Hou, X. Ma and Z. Gao, *Journal of Colloid and Interface Science*, 2026, **702**, 138835.
19. H. B. Lian, R. M. Hu, L. Zheng, D. W. Gao, S. Wang, R. Y. Wang, B. Wang and G. Z. Chen, *Journal of Catalysis*, 2025, **444**, 116003.
20. X. Liu, X. Liu, J. Zhao, M. Ban, S. Wu and F. Liu, *Journal of Colloid and Interface Science*, 2026, **702**, 138976.
21. Q. Lv, J. Yi, J. C.-H. Lam, H. Wang, H. Zhang, S. Huang and Y. Luo, *ACS Sustainable Chemistry and Engineering*, 2025, **13**, 1677-1688.
22. H. M. Wen, Z. Y. Fan, S. Dou, J. C. H. Lam, W. J. Zhang and Z. P. Chen, *Inorganic Chemistry Frontiers*, 2024, **11**, 4449-4458.